Facile fabrication of Fe-BDC/Fe-2MI heterojunction with boosted photocatalytic activity for Cr(VI) reduction

Qin He [a], Yangjie Fu [a], Xueying Ge [b], Abdullah M. Al-Enizi [c], Ayman Nafady [c], Qi Wang [a],*, Shengqian Ma [b],*

[a] School of Environmental Science and Engineering, Zhejiang Gongshang University, Hangzhou 310018, China
[b] Department of Chemistry, University of North Texas, 1508 W Mulberry St, Denton, TX 76201, USA
[c] Chemistry Department, College of Science, King Saud University, Riyadh 11451, Saudi Arabia

ARTICLE INFO

ABSTRACT

Novel Fe-BDC/Fe-2MI heterojunction (H_2BDC: terephthalic acid, 2MI: 2-methylimidazole) was prepared via a one-pot solvothermal method. Herein, mixed ligands (H_2BDC and 2MI) was applied to form complex with Fe(III). Interestingly, the presence of 2MI can regulate the structure of Fe-BDC. Spindle-like MIL-88B(Fe) was observed in Fe-BDC/Fe-2MI composite, while MIL-53(Fe) was identified in naked Fe-BDC. By employing photo-electrochemical characterizations, Fe-BDC/Fe-2MI was optimized at an initial molar ratio of 1:0.5:10 for Fe(III):H_2BDC:2MI, which exhibited the highest photocurrent response, lowest charge transfer resistance, and fastest surface reaction kinetics as compared to the individual Fe-BDC and Fe-2MI. Due to the formation of the heterojunction which lead to beneficial photoelectrochemical properties, the as-prepared samples exhibited boosted photocatalytic activity for Cr(VI) reduction. The calculated pseudo-first-order rate constant (k) was 0.046 min^{-1} for Fe-BDC/Fe-2MI, which was 15.3 and 6.6 times that of Fe-BDC (0.003 min^{-1}) and Fe-2MI (0.007 min^{-1}), respectively. Moreover, the optimized Fe-BDC/Fe-2MI demonstrated superior performance with negligible loss in activity after 4 cyclic runs.

1. Introduction

In the 21st century, safeguarding the environment has become one of the most important factors for further development of human race. As for the profound purification of wastewater and sewage, traditional technologies have been unable to meet the growing demands that are supplemented by stricter standards. There is an urgent need for developing novel approaches. Heterogeneous photocatalysis was first observed in TiO_2; since then it has been intensively studied and proved to be environmentally friendly for extensive treatment [1,2]. Upon proper light irradiation ($E_{light} > E_{band\ gap}$), electron—hole ($e^-$—$h^+$) pairs can be generated in the conduction band (CB) and valence band (VB) of a semiconductor photocatalyst. The active e^- and h^+ can be captured by molecules such as O_2, H_2O, and various pollutants, leading to the initiation of reduction and oxidation, respectively. In this way, photocatalysis can be utilized for the disposal of various impurities such as heavy metal ions and refractory organic pollutants. For more efficient use of solar energy, incessant attention has been paid to novel photocatalytic materials that exhibit high efficiency under the visible range or sunlight [3–6].

Similar to traditional semiconductors with delocalized CB and VB, metal–organic frameworks (MOFs) can be identified as novel crystalline molecular photocatalysts that possess the lowest unoccupied molecular orbital (LUMO) and highest occupied molecular orbital (HOMO) [7–9]. Since the first report of MOF-5 for photocatalytic degradation of phenol in 2007, MOFs-based photocatalysis has garnered increasing attention in the past decade [10–15]. Herein, MOFs can be built using the versatile connection between metal ions/clusters and organic linkers [16]. For example, high-valent metal ions (Ti^{4+}, Zr^{4+}, Fe^{3+}, Al^{3+} or Cr^{3+}) were frequently applied to complexes with carboxylates, which led to the formation of stable MOFs. Besides, there is a probability that divalent metal ions (Zn^{2+}, Cu^{2+}, Co^{2+} or Ni^{2+}) react with azolates. In this regard, the representative MOFs (MIL, UiO, and ZIF series) were prepared [17]. However, most MOFs exhibited a wide band gap ($E_{HOMO-LUMO} > 3.1$ eV) that can only respond to UV light. For example, the $E_{HOMO-LUMO}$ for UiO-66(Zr), MIL-125(Ti), and MOF-5(Zn) were ca. 3.9 eV, 3.6 eV, and

---

Scheme 1. Schematic for the preparation of Fe-BDC/Fe-2MI.

3.4 eV, respectively [18–21].

Among the various kinds of MOFs, Fe-MOFs with lower $E_{HOMO-LUMO}$ (< 2.9 eV) are extremely appealing; these are composed of earth-abundant Fe and a hard Lewis base (such as carboxylates). The presence of extensive Fe–O clusters can lead to an enhanced absorption of visible light. By modifying the organic ligands, such as terephthalic acid (H$_2$BDC), benzene-1,3,5-tricarboxylic acid (H$_3$BTC), and fumaric acid (H$_2$FUM), different kinds of Fe-MOFs (MIL-53, MIL-100 and MIL-88A) can be fabricated. Besides, the structure of Fe-MOFs can also be engineered by altering the preparation conditions (such as temperature, pH, and initial molar ratio). For example, using H$_2$BDC as the organic ligand, visible-light-active Fe-MOFs (MIL-53, MIL-68, MIL-88B and MIL-101) with different structures were reported and subsequently applied for environmental remediation. For example, simultaneous reduction of Cr(VI) and oxidation of dyes can be observed with MIL-53(Fe) [22]. Further, MIL-68(Fe) can also work as an efficient photocatalyst for the treatment of Cr(VI) and malachite green [23]. Spindle-like MIL-88B(Fe) with uniform size and morphology demonstrated good photocatalytic activity for the degradation of methylene blue and rhodamine B dyes [24]. Besides, bisphenol A can be efficiently photodegraded by MIL-101 (Fe) with the presence of persulfate. Despite of the above-mentioned factors, these naked Fe-MOFs are still hindered by low efficiency due to the rapid recombination of e$^-$—h$^+$ pairs.

To address this issue, fabrication of a heterojunction was proven to be an effective way [25]. Typically, Fe-MOFs can be coupled with other photocatalysts. When their CB-VB or LUMO-HOMO positions correspond with each other, the e$^-$—h$^+$ pairs can be more efficiently separated, leading to enhanced photocatalytic performance. For example, visible-light-active semiconductors (WO$_3$ [26], Fe$_2$O$_3$ [27], AgI [28], Ag$_3$PO$_4$ [29], C$_3$N$_4$ [30,31]) were frequently reported to form heterojunctions with Fe-MOFs. In addition to MOFs/semiconductor heterojunctions, the construction of MOFs/MOFs heterojunction has recently attracted increasing interest. More and more MOFs/MOFs have been reported, including Co-BPDC/Co-BDC [32], NH$_2$-UiO-66@MIL-101(Fe) [33], MIL-101(Cr)@NH$_2$-MIL-125(Ti) [34], ZIF-8/ZIF-67 [35], and etc. For example, MIL-100(Fe)/MIL-53(Fe) with different organic linkers (H$_3$BTC and H$_2$BDC) were fabricated via a two-step procedure, and displayed enhanced activity for the degradation of Microcystin-LR (MC-LR) as compared to single MIL-100(Fe) or MIL-53(Fe) [36]. In this way, the merits of individual MOFs as well as incorporate new properties can be maintained or promoted. Magnetic recyclable Fe$_3$O$_4$@HKUST-1/MIL-100(Fe) with the same H$_3$BTC ligand can not only promote the photocatalytic degradation of methylene blue dye, but also regulate the specific surface and interior pore size [37].

In this study, novel Fe-MOFs (Fe-BDC/Fe-2MI) were prepared via a one-pot solvothermal method using terephthalic acid (H$_2$BDC) and 2-methylimidazole (2MI) as mixed ligands. By changing the initial molar ratio of Fe(III):H$_2$BDC:2MI, Fe-BDC/Fe-2MI heterojunctions with variable structures were obtained. The performance of Fe-BDC/Fe-2MI were evaluated for the photocatalytic reduction of Cr(VI) and compared to that of naked Fe-BDC and Fe-2MI. Further, intensive studies were performed to investigate the effect of the initial Fe(III) source, solution pH,

catalyst dosage, coexisting organic compounds and inorganic salts. The cyclic stability of the optimized Fe-BDC/Fe-2MI was also tested. Based on the values of $E_{HOMO-LUMO}$ and results obtained using flat band measurements, a tentative mechanism for the electron separation and transfer processes were presented.

2. Experimental

2.1. Chemicals

FeCl$_3$.6H$_2$O, Fe(NO$_3$)$_3$.9H$_2$O, Fe$_2$(SO$_4$)$_3$, FeCl$_2$.4H$_2$O with analytic grades were purchased from Chengdu Kelong Chemical Reagent Co., Ltd. Further, 2-Methylimidazole (2MI), 1,4-benzenedicarboxylic acid (H$_2$BDC), and N, N-Dimethylformamide (DMF) were purchased from Aladdin Reagents Co., Ltd. All reagents were used as received without further purification.

2.2. Synthesis details

2.2.1. Preparation of Fe-BDC and Fe-2MI

Fe-BDC was prepared via a solvothermal method, which has been stated in previous reports [38,39]. Using a typical procedure, 4 mmol FeCl$_3$.6H$_2$O and 4 mmol H$_2$BDC were dissolved in 30 mL DMF separately. Subsequently, the H$_2$BDC solution was added dropwise to the FeCl$_3$.6H$_2$O solution. After constant stirring at room temperature for 30 min, the above mixture was transferred to a Teflon-lined vessel and heated at 150 for 15 h. After cooling to room temperature, the precipitate was separated via centrifugation; this was followed by a thorough washing with ethanol and deionized water. Finally, the yellow powder was dried overnight at 60 . The as-prepared sample was denoted as Fe-BDC. For the preparation of Fe-2MI, the procedure was the same as that of Fe-BDC; however, in this case, 40 mmol 2MI was applied instead of H$_2$BDC in the initial step.

2.2.2. Preparation of Fe-BDC/Fe-2MI

Similarly, as shown in Scheme 1, Fe-BDC/Fe-2MI composites with different initial molar ratios of Fe(III):H$_2$BDC:2MI were prepared via the above solvothermal procedure. Herein, the initial amount of FeCl$_3$.6 H$_2$O (4 mmol) remained the same, while the amount of the ligand varied from 1 mmol to 4 mmol and 4–40 mmol for H$_2$BDC and 2MI, respectively. In this way, a series of Fe-BDC/Fe-2MI samples were prepared with the different ratio of 1:0.25:10, 1:0.75:10, 1:1:10, 1:1:1, and 1:1:5. Especially, as for Fe-BDC/Fe-2MI with the optimal ratio of 1:0.5:10, 2 mmol H$_2$BDC and 40 mmol 2MI were dissolved together in 30 mL DMF, called Fe-BDC/Fe-2MI. After the incorporation of similar solvothermal procedure as well as washing and drying processes, Fe-BDC/Fe-2MI powder with an orangish-yellow color was obtained.

2.3. Characterizations

Powder X-ray diffraction (XRD) patterns were obtained using a Bruker D8 diffractometer with Cu Kα radiation. Fourier-transform
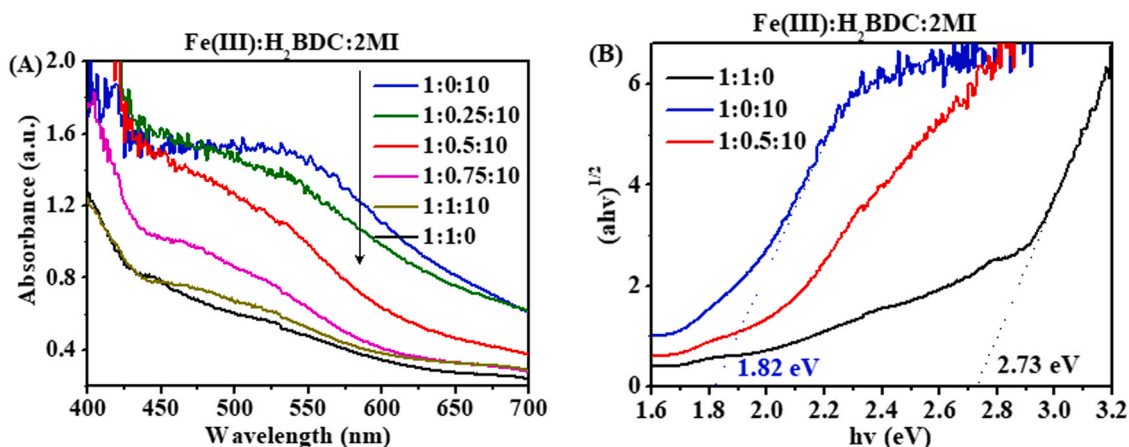
Fig. 1. (A) UV-Vis DRS spectra and (B) estimated band gaps of the as-prepared Fe-based sample.

infrared (FT-IR) spectra were recorded on a Bruker VERTEX 70 spectrometer. Nitrogen (N_2) adsorption/desorption isotherms were collected using a Quantachrome Autosorb-IQ analyzer at 77 K. The specific BET surface areas (S_{BET}) were calculated using the Brunauer-Emmett-Teller method. X-ray photoelectron spectroscopy (XPS) was measured on a VG Thermo Escalab 220i-XL with Al Kα radiation. Scanning electron microscopy (SEM) images were mapped on a Hitachi S-4800 microscope. UV-Visible diffuse reflectance spectra (UV-Vis DRS) were recorded using a TU-1901 UV-Vis spectrophotometer. Photocurrent response, electrochemical impedance spectroscopy (EIS), and Mott-Schottky (M-S) plots were measured using a CHI 660E electrochemical station.

2.4. Evaluation of photocatalytic performance

The photocatalytic performance of the as-prepared Fe-containing samples were evaluated via the reduction of Cr(VI) under visible light (λ ≥ 420 nm). The light source was a 300 W Xe lamp (CEL-300, Beijing Zhongjiao Jinyuan Co., Ltd.) with an ultraviolet filter. The intensity of visible light was ca 0.100 mW/cm^2. Typically, unless specified, the as-prepared sample powder (10 mg) was dispersed into 100 mL of an aqueous solution of Cr(VI) (80 μmol/L) with the presence of EDTA-2Na (2 mmol/L) at unadjusted pH. Prior to irradiation, the suspension was stirred in the dark for 30 min to achieve adsorption-desorption equilibrium. At given time intervals, the suspension was collected and separated by filtration. According to our previous reports, the 1,5-diphenylcarbazide colorimetry method was applied to measure the concentration of Cr(VI) in the supernatant. Further, the purple complex of Cr (VI)− 1,5-diphenylcarbazide was monitored at 540 nm by a UV2012PC spectrophotometer.

3. Results and discussion

3.1. Optical and photoelectrochemical properties

As a photocatalyst, optical absorption is of vital importance for photocatalysis; this is because it determines the accurate utilization of incident light. Thus, to elucidate the optical properties, UV-Vis-DRS spectra were measured and the corresponding results were obtained (Fig. 1A). Herein, Fe-BDC/Fe-2MI samples were prepared with different initial molar ratios of Fe(III):H$_2$BDC:2MI. It was observed that Fe-BDC/Fe-2MI prepared with the ratio of 1:0:10 (Fe-2MI) exhibited the highest absorption in the region of visible light (400–700 nm), while the sample with the ration 1:1:0 (Fe-BDC) displayed the lowest absorption. Moreover, once the initial molar ratio of Fe(III):2MI was fixed at 1:10, increasing the concentration of H$_2$BDC lead to a decrease in the absorption. As shown in Fig. S1, the colors of 1:1:0 (Fe-BDC) and 1:0:10 (Fe-2MI) samples were yellow and brown, respectively. As for Fe-BDC/

Fe-2MI (1:0.5:10) with mixed ligands, the color was reddish brown. After the Kubelka-Munk conversion [40,41], the band gaps (E_g) of the as-prepared Fe-BDC/Fe-2MI samples were obtained (Fig. 1B). For example, the corresponding E_g of pure Fe-BDC (1:1:0) and Fe-2MI (1:0:10) were estimated to be 2.73 eV and 1.82 eV, respectively.

Generally, the photocatalytic performance of a photocatalyst is associated with the generation, separation, and transfer of light-induced electron-hole (e^-—h^+) pairs. Herein, the as-prepared sample powders were loaded onto F-doped tin oxide (FTO) glass as film electrodes for photoelectrochemical measurements. For example, photocurrent response under chopped visible light were measured in a mixed solution of Na$_2$SO$_4$ and Na$_2$SO$_3$. As shown in Fig. 2A, the photocurrent density on Fe-BDC/Fe-2MI was in the order of 1:0.5:10 > 1:0.75:10 > 1:0.25:10, among the tested samples, Fe-BDC/Fe-2MI with the initial ratio of 1:0.5:10 displayed the highest photocurrent density; this indicates the easiest generation of e^-—h^+ pairs under visible light. As compared to Fe-BDC (1:1:0) and Fe-2MI (1:0:10) having single organic ligands (Fig. 2B), Fe-BDC/Fe-2MI with mixed ligands displayed significantly enhanced photocurrent response.

To elucidate the reasons for the above phenomenon, the factors that associated with the generation, separation, and transfer of photogenerated e^-—h^+ pairs were further investigated. For example, enhanced visible light absorption usually resulted in an easier generation of e^-—h^+ pairs. As shown in Fig. 1A, the visible light absorption was in the order of Fe-2MI > Fe-BDC/Fe-2MI > Fe-BDC. It was observed that Fe-2MI displayed the highest visible light absorption rather than Fe-BDC/Fe-2MI. Thus, the highest photocurrent response of Fe-BDC/Fe-2MI cannot simply be ascribed to the enhanced generation of e^-—h^+ pairs. Furthermore, the current response was measured in an electrolyte of Na$_2$SO$_4$ with the addition of H$_2$O$_2$ as hole scavenger. In this way, the surface reaction kinetics can be deduced [42,43]. As shown in Fig. 2C and D, the highest current density was observed with Fe-BDC/Fe-2MI under dark as well as light conditions; this signified the fast reaction kinetics on the catalyst surface. Moreover, EIS Nyquist plots were also measured to investigate the capacitance and resistance. As shown in Fig. 2E , the radius of the semicircle was in the order of Fe-2MI > Fe-BDC > Fe-BDC/Fe-2MI. According to the principle of EIS, smaller radius corresponds to a lower charge transfer resistance [44]. In addition to surface reaction and charge transfer properties, the recombination properties of photogenerated charges were also estimated via the transient photocurrent. As shown in Fig. S2, the Fe-BDC/Fe-2MI composite displayed the slowest recombination rate. Therefore, it can be deduced that the separation and transfer of photogenerated charges were significantly promoted in Fe-BDC/Fe-2MI with mixed ligands. The reason can be ascribed to the formation of heterojunctions between n-type Fe-BDC and Fe-2MI. Further, ESI Nyquist plots of Fe-BDC/Fe-2MI before and after visible light irradiation were also compared. As shown
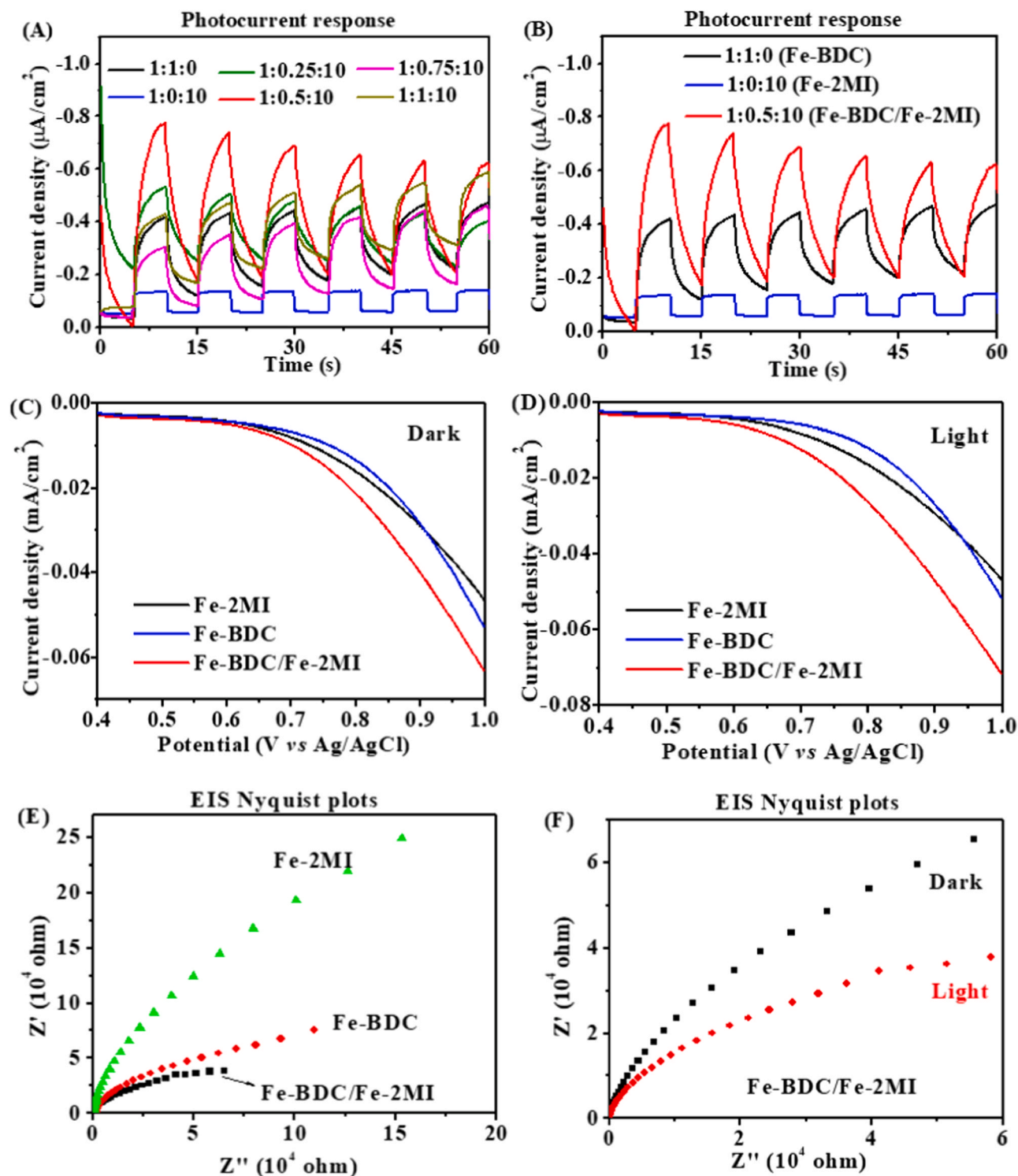
Fig. 2. (A) and (B) Photocurrent response of the as-prepared samples under chopped visible light; comparison of I-V curves under (C) dark and (D) light conditions in 0.5 M H$_2$O$_2$. (E) ESI Nyquist plots of Fe-BDC, Fe-2MI and Fe-BDC/Fe-2MI under visible light; (F) ESI Nyquist plots of Fe-BDC/Fe-2MI before and after visible light irradiation.

in Fig. 2F, the impedance was significantly decreased under visible light irradiation; this indicated the positive effect of light in accelerating the process of charge transfer.

3.2. Morphological and structural characterizations

SEM analysis was carried out to investigate the possible changes in morphology and particle size. As shown in Fig. 3A, the particle size was less than 1 μm for Fe-BDC. Whereas, the presence of 2MI significantly altered the structure of Fe-BDC. Uniform hexagonal microrods can be observed in Fe-BDC/Fe-2MI (Fig. 3C). The average size was ca. 6 μm in length and 2 μm in diameter. Moreover, pure Fe-2MI displayed a spherical shape with size ranging from ca. 1–2 μm. TEM analysis and EDS mapping were further carried out to investigate the structure as well
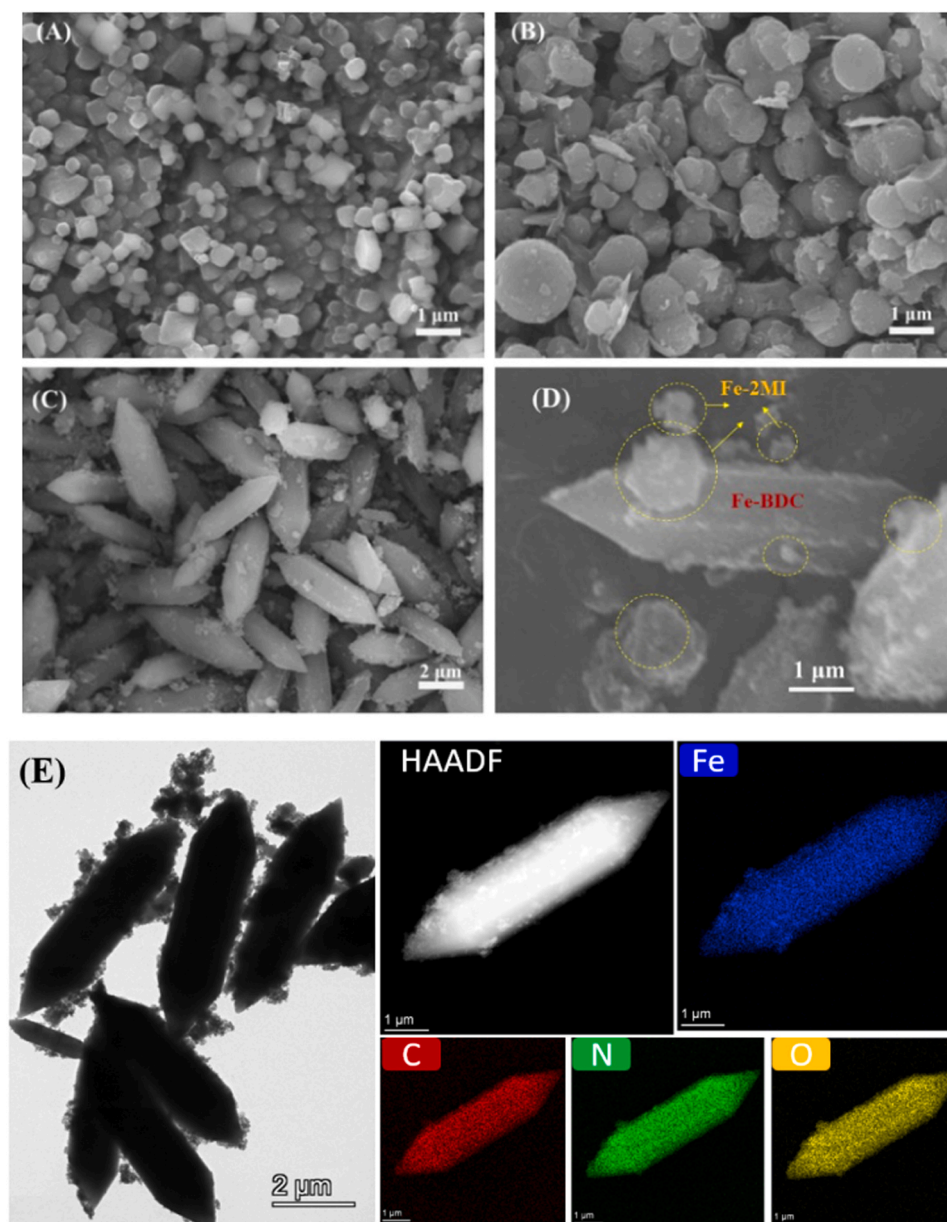
Fig. 3. SEM images of (A) Fe-BDC, (B) Fe-2MI, (C) and (D) Fe-BDC/Fe-2MI; (E) TEM of Fe-BDC/Fe-2MI, HAADF image, and EDS elemental maps of Fe, C, N and O.

as elemental composition of Fe-BDC/Fe-2MI (Fig. 3E). It can be observed that Fe, C, N and O elements were evenly distributed. Besides, the solid state and larger size led to decreased BET surface area. For example, the values of Fe-BDC and Fe-BDC/Fe-2MI were measured to be 124.5 and 66.6 m^2/g, respectively (Fig. S3). In order to find out the proportion of the two components, the changing trend was speculated from the yields of Fe-BDC/Fe-2MI with different initial molar ratios (Fig. S4). After adding H_2BDC to the initial precursors of Fe-2MI, the catalyst yield was gradually increased. Maximum Fe-BDC/Fe-2MI yield was obtained when the initial molar ratio of Fe(III):H_2BDC:2MI was 1:0.5:10.

In addition to morphology change, the PXRD patterns of Fe-BDC were also greatly altered by the presence of 2MI (Fig. 4), indicating different phase composition. The main peaks of Fe-BDC and Fe-BDC/Fe-2MI were similar to that of MIL-53(Fe) and MIL-88(Fe), respectively [45–47]. In order to confirm the structure of Fe-BDC and monitor the structural changes of Fe-BDC/Fe-2MI, FT-IR analysis were further performed (Fig. 5).

As for pure H_2BDC (curve a), characteristic peaks of Ar-C-H (726 cm^{-1}), C-O (1503 and 1416 cm^{-1}), and C=O (1637 cm^{-1}) can

be observed. After forming a complex with Fe(III), the adsorption band of carboxyl group shifted from 1637 cm^{-1} to 1601 cm^{-1}. Further, the peaks at 1516 cm^{-1} and 1393 cm^{-1} are associated with ν_s and ν_{as} of the C-O band in the carboxyl group of the H_2BDC linker, respectively. Meanwhile, the peak at 550 cm^{-1} was ascribed to the stretching vibration of the Fe-O bond. Thus, it can be deduced that a Fe-oxo cluster was formed between Fe(III) and the carboxyl group of H_2BDC. As for Fe-BDC/2MI, the corresponding peaks exhibited some shift. For example, the Fe-O bond appeared at 538 cm^{-1}, which was lower than that in Fe-BDC (550 cm^{-1}). Accordingly, characteristic peaks shifted to 1506 and 1385 cm^{-1} for C-O and 1589 cm^{-1} for C=O. However, the characteristic peaks of C=N (ca. 1600 cm^{-1}) in 2MI were overlapped with the broad peak of C=O. Further, only tiny peaks (1056 and 985 cm^{-1}) of C-N in the imidazole ring were observed [48]. In order to confirm the presence of 2MI, the Fe-2BDC/Fe-2MI powder was dissolved by DCl and investigated by ^{1}H NMR with DMSO as the solvent. In addition to a strong signal of H in the aromatic ring (H_2BDC), peaks in accordance with H in –CH_3 and imidazole ring can also be observed (Fig. S5).

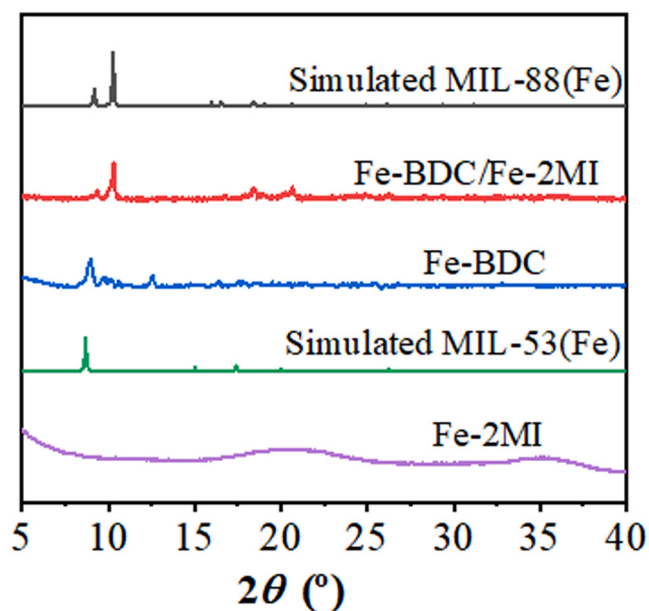As for the Fe-BDC/Fe-2MI composite, XPS analysis was further

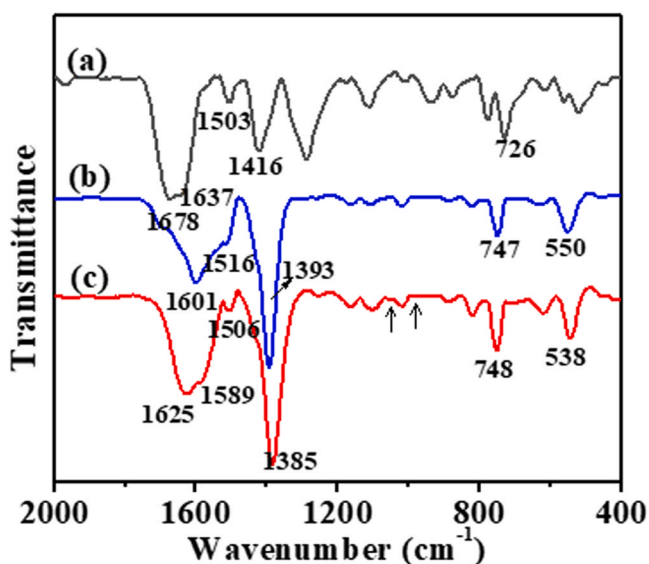**Fig. 4.** PXRD patterns of different Fe-based samples.

Fig. 5. FT-IR spectra of (a) H$_2$BDC, (b) Fe-BDC and (c) Fe-BDC/Fe-2MI.

performed to investigate the elemental compositions and states on its surface. As shown in Fig. 6, obvious signals of Fe 2p, C 1 s, N 1 s and O 1 s can be observed. As for Fe 2p (Fig. 6A), the major peaks at 710.5 eV and 724.3 eV were ascribed to Fe 2p3/2 and 2p1/2, respectively. Moreover, the corresponding satellite peaks can also be observed at ca. 718.3 eV and 730.8 eV, respectively. As for C1s (Fig. 6B), the XPS peak can be deconvolved into several corresponding peaks. For example, the main peak at 284.1 eV was ascribed to the sp2 hybrid carbon of C-C and C=C. Further, the small peaks at 285.4 eV and 287.8 eV corresponded to N-C=N and C-N, respectively; these probably originated from the 2MI ligand. Consistent with the results in C 1 s spectra, the N 1 s spectra (Fig. 6C) further confirmed the presence of pyridine-N from the imidazole ring. Because mixed ligands (H$_2$BDC and 2MI) were used in Fe-BDC/Fe-2MI, the high resolution O1s spectra were further obtained to reveal the presence of O=C from H$_2$BDC and O-Fe from metallic clusters. As shown in Fig. 6D, the peaks at 531.5 eV, 530.6 eV, and 529.3 eV correspond to C=O, –OH, and Fe–O, respectively [49].
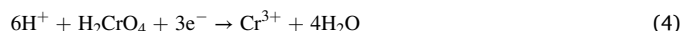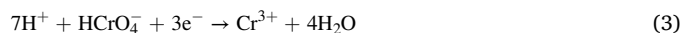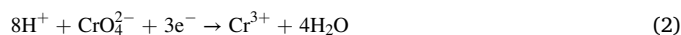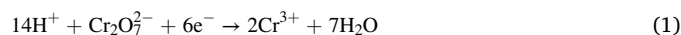
3.3. Photocatalytic reduction of Cr(VI)

Electroplating, tanning, printing and dyeing industries will produce a large number of chromium containing wastewaters. Typically, the migratable and carcinogenic Cr(VI) was reduced to Cr(III), which is 100 times less toxic and easy to form Cr(OH)$_3$ precipitate. In industry, high concentration of Cr(VI) is reduced by adding reducing agent. However, due to solubility product limit, secondary salt pollution, and etc., novel technologies need to be developed. Photocatalysis, which can utilize solar energy, is considered to be one of the most promising technologies for treating Cr(VI)-containing wastewater.

In this study, Fe-BDC/Fe-2MI samples with different initial molar ratio of Fe(III):H$_2$BDC:2MI were prepared via a solvothermal procedure. The photocatalytic performance of the as-prepared samples were evaluated and compared via the reduction of Cr(VI) under visible light. With a 0.1 g/L catalyst dosage and an unadjusted initial solution pH, Cr(VI) reduction dynamics using different photocatalysts were observed and compared in Fig. 7A. After visible light irradiation for 90 min, the efficiency for Cr(VI) reduction was only 22.8% and 49.2% with 1:1:0 (Fe-BDC) and 1:0:10 (Fe-2MI), respectively. Once mixed ligands with both H$_2$BDC and 2MI were applied to form a complex with Fe(III), the photocatalytic performance was dramatically enhanced. For example, when the ratio of Fe(III):H$_2$BDC:2MI was 1:0.25:10, the efficiency for Cr(VI) reduction can reach 92.7% in 90 min, when the ratio of Fe(III): H$_2$BDC:2MI is 1:0.5:10, the efficiency can almost reached reach 100% in 60 min. It was observed that with increasing initial concentration of H$_2$BDC, the photocatalytic performance was further enhanced and an optimal activity was achieved for Fe-BDC/Fe-2MI with the ratio of 1:0.5:10.

In this research, the effect of adjusting initial 2MI concentration was also studied. As shown in Fig. S6, similar rate enhancement can be observed when compared with pure Fe-BDC and Fe-2MI. The reduction of Cr(VI) on Fe-BDC/Fe-2MI was in the order of 1:1:5 > 1:1:10 > 1:1:1. Despite of this, Fe-BDC/Fe-2MI (1:0.5:10) still exhibited the highest performance. Moreover, reduction of Cr(VI) followed first-order kinetics. The pseudo-first-order rate constants (k) were calculated and shown in Fig. 7B. The value was 0.046 min^{-1} with optimized Fe-BDC/ Fe-2MI, which was 15.3 and 6.6 times than that of Fe-BDC (0.003 min^{-1}) and Fe-2MI (0.007 min^{-1}), respectively. Therefore, a distinct synergistic effect can be deduced with Fe-BDC/Fe-2MI having mixed ligands. Hereafter, unless otherwise mentioned, Fe-BDC/Fe-2MI (1:0.5:10) was applied for further experimentation.

In addition to the combination and concentration of organic ligands (H$_2$BDC and 2MI), the effect of Fe(III) sources on Cr(VI) reduction dynamics was also investigated. Fe-BDC/Fe-2MI with the optimal ratio of 1:0.5:10 ratio was prepared using different types of Fe(III) sources, including FeCl$_3$, Fe(NO$_3$)$_3$, Fe$_2$(SO$_4$)$_3$, and FeCl$_2$. As shown in Fig. 8A, FeCl$_3$ as the starting Fe(III) source exhibited the highest performance. Furthermore, using optimized Fe-BDC/Fe-2MI as the photocatalyst, the effect of operating factors such as solution pH, catalyst dosage, coexisting organic compounds and inorganic species were investigated in detail. For example, the effect of the initial solution pH on Cr(VI) reduction was studied. As shown in Fig. 8B, acidic pH was beneficial for Cr(VI) reduction. The reduction of Cr(VI) followed the order of pH 2 > pH 3 > pH 4.5 > pH 6 > pH 8. The phenomena can be ascribed to the following aspects [41,44]. First, regardless of the Cr(VI) existing states (Cr$_2$O$_7^{2-}$, CrO$_4^{2-}$, HCrO$_4^-$ or H$_2$CrO$_4$), H$^+$ was always consumed during the reduction of Cr(VI) according to Eq. (1)–(4):

$$14H^+ + Cr_2O_7^{2-} + 6e^- \rightarrow 2Cr^{3+} + 7H_2O \qquad (1)$$

$$8H^+ + CrO_4^{2-} + 3e^- \rightarrow Cr^{3+} + 4H_2O \qquad (2)$$

$$7H^+ + HCrO_4^- + 3e^- \rightarrow Cr^{3+} + 4H_2O \qquad (3)$$

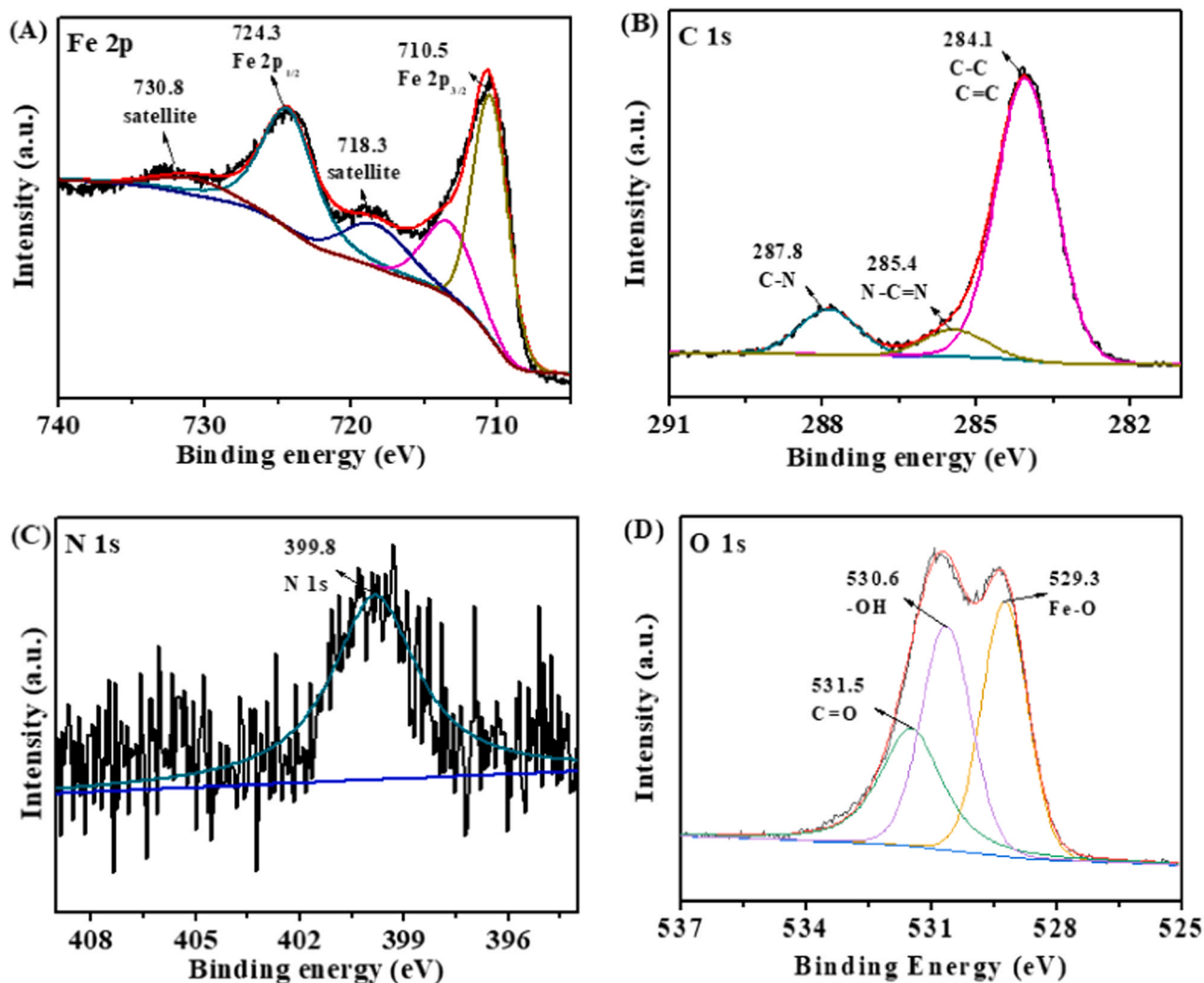$$6H^+ + H_2CrO_4 + 3e^- \rightarrow Cr^{3+} + 4H_2O \qquad (4)$$

Fig. 6. High-resolution XPS spectra of Fe-BDC/Fe-2MI: (A) Fe 2p, (B) C 1s, (C) N 1s and (D) O 1s.
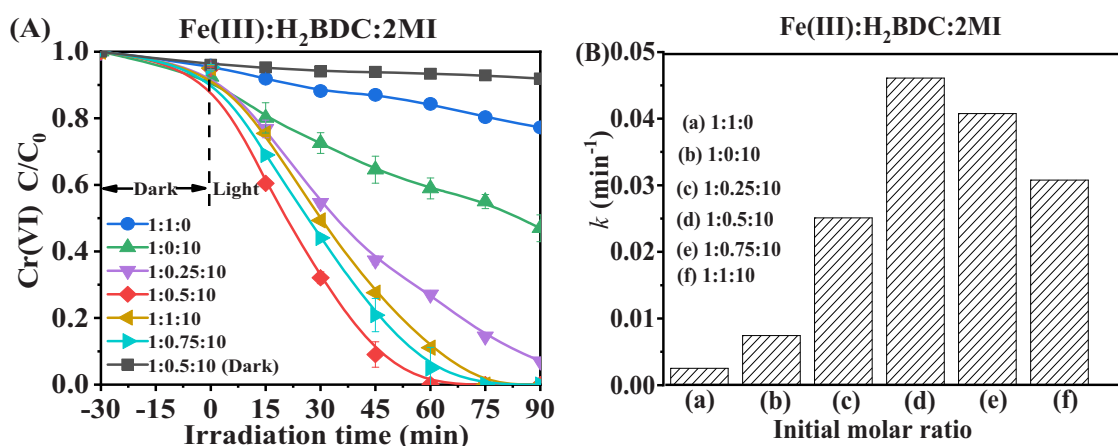

Fig. 7. Photocatalytic reduction of Cr(VI) under different conditions: (A) Cr(VI) adsorption and reduction dynamics, (B) corresponding rate constants.

Therefore, higher H$^+$ concentration (lower pH) will be beneficial for the reaction. Second, with decreasing pH, the thermodynamic driving force increased by 79 mV/pH due to the difference in changes of $E_{Cr(VI)/Cr(III)}$ and E_{CB} as a function of pH. Besides, strong acidic condition was unfavorable for the stability of Fe-MOFs. Too acidic pH may offset the

impact induced by thermodynamic driving force.

Catalyst dosage was another important operating factor that needs to be optimized for future large-scale applications. As shown in Fig. 8C, the effect of catalyst dosage (0.05–0.3 g/L) on Cr(VI) reduction was studied. Even at very low concentration of Fe-BDC/Fe-2MI (0.05 g/L), the
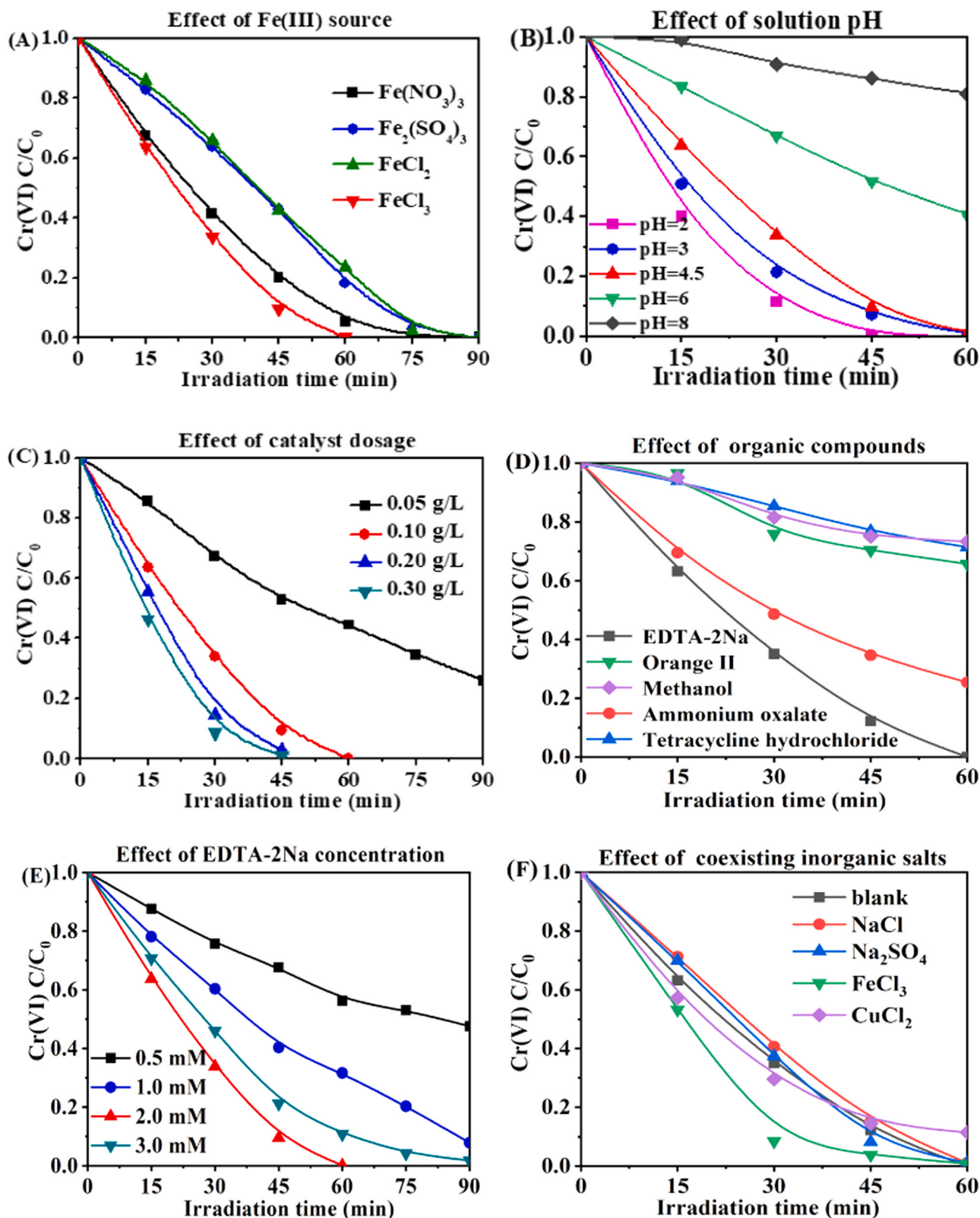
Fig. 8. Effect of (A) Fe(III) source, (B) solution pH, (C) catalyst dosage, (D) coexisting organics, (E) EDTA-2Naconcentration and (F) coexisting inorganic salts on the photocatalytic reduction of Cr(VI) using Fe-BDC/Fe-2MI as photocatalyst.

removal efficiency for Cr(VI) reached ca. 89% after 90 min of visible light irradiation. A significantly enhanced performance can be observed when the catalyst dosage was increased to 0.1 g/L. Once the dosage exceeds this value, such as 0.2 g/L and 0.3 g/L, a slower increasing rate

was observed for the Cr(VI) reduction despite of a higher performance. Besides, 0.1 g/L was frequently applied in previous reports by MOFs-based heterojunctions [50]. Thus, for economic considerations, 0.1 g/L was chosen for the following studies.
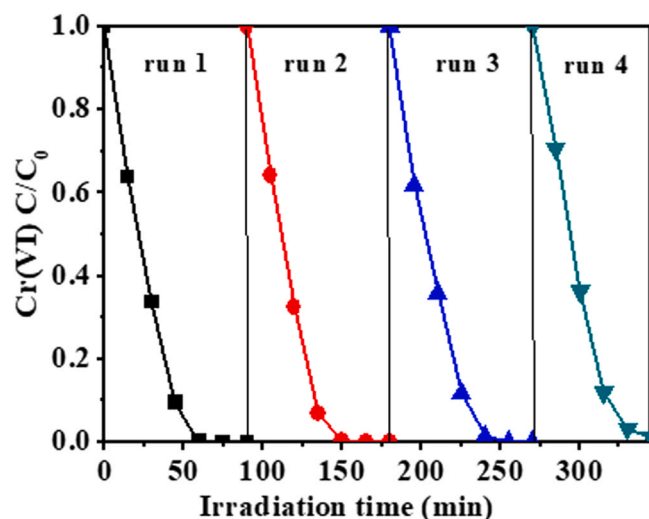
Fig. 9. Stability of Fe-BDC/Fe-2MI for Cr(VI) reduction in cyclic runs at unadjusted pH.

In actual Cr(VI)-containing wastewaters, it is coexisting organic matters that increases the difficulty for Cr(VI) disposal using traditional approaches. For example, EDTA was extensively applied in industrial processes including printed circuit boards, photography, and paper agrochemicals. Herein, the effect of different coexisting organics was investigated, such as EDTA-2Na (2 mmol/L), ammonium oxalate (0.3 mmol/L), methanol (10 mmol/L), Tetracycline hydrochloride (20 mg/L) and orange II (0.1 mmol/L). It can be observed from Fig. 8D that the presence of EDTA-2Na displayed highest performance. The reason may be ascribed to the role of EDTA-2Na as a hole scavenger, leading to more efficient separation of e^-—h^+ pairs. In this way, the photo-generated electrons in the LUMO of Fe-BDC/Fe-2MI can be more efficiently captured by Cr(VI). Besides, the reduction of Cr(VI) was accelerated with the increasing concentration of EDTA-2Na (Fig. 8E).

In addition to coexisting organics, inorganics were also included in actual chromium-containing wastewater. Thus, the effect of inorganics were further studied by adding different inorganic salts, such as NaCl (0.015 mol/L), Na_2SO_4 (0.015 mol/L), $FeCl_3$ (0.01 mol/L) and $CuCl_2$ (0.01 mol/L). The results were shown in Fig. 8F. It can be observed that the presence of inorganic salts has negligible negative effects on the photocatalytic reduction of Cr(VI). Besides, the presence of $FeCl_3$ even has promoting effect. Thus, for comprehensive consideration, Fe-BDC/
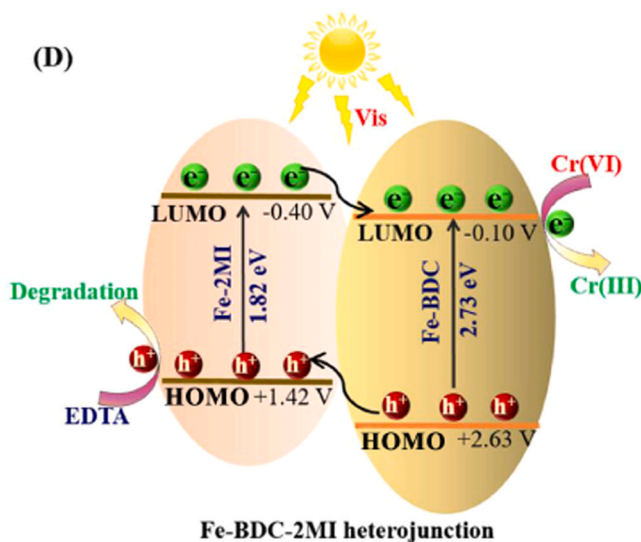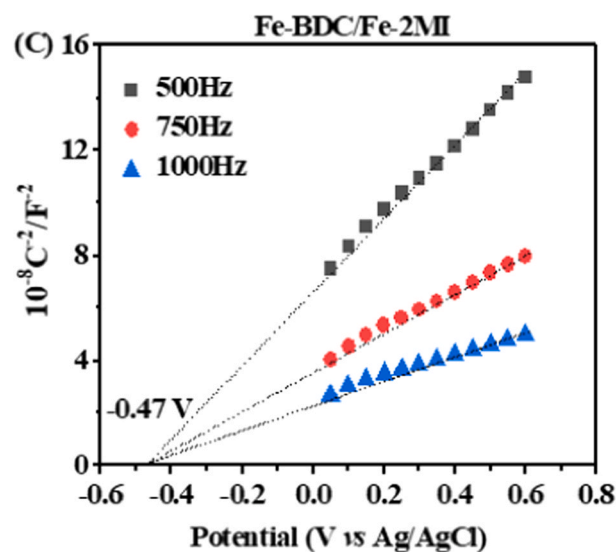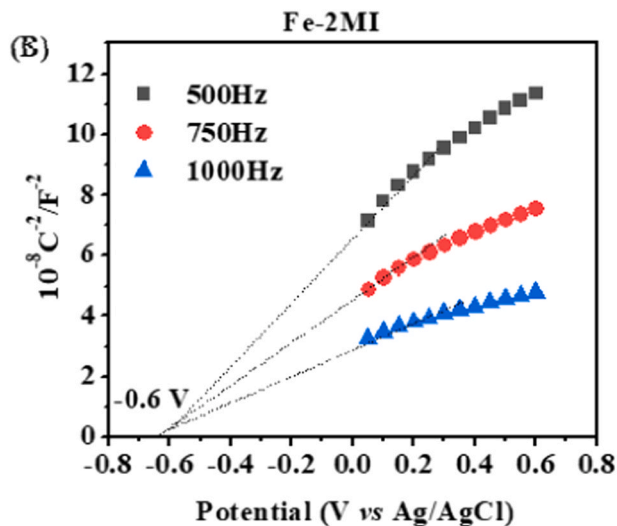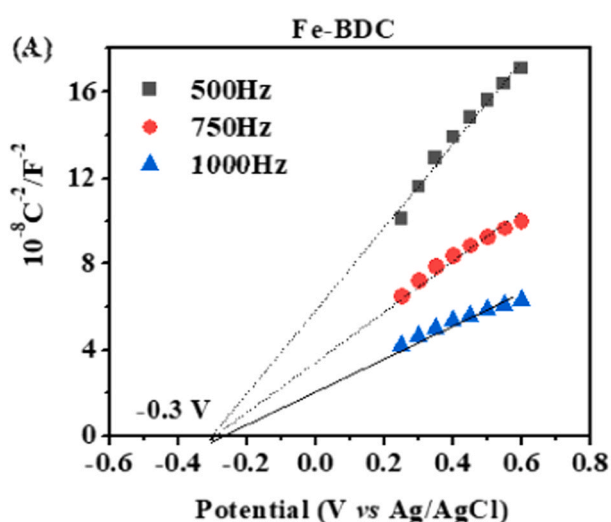

Fig. 10. Mott-Schottky plots of (A) Fe-BDC, (B) Fe-2MI and (C) Fe-BDC/Fe-2MI; (D) Proposed mechanism for charge separation in Fe-BDC/Fe-2MI heterojunction under visible light irradiation.

Fe-2MI has great potential for future real environmental applications.

Based on the above analysis, Fe-BDC/Fe-2MI prepared from $FeCl_3$ with the ratio of 1:0.5:10 of $Fe(III):H_2BDC:2MI$ was selected as the optimal photocatalyst in this study. In addition to the high performance of Fe-BDC/Fe-2MI, its stability was also a vital factor. In this work, the stability of Fe-BDC/Fe-2MI was evaluated by both cyclic runs and Fe^{3+} leaching content. The concentration of leached Fe^{3+} was monitored using 1,10-phenanthroline colorimetric method ($\lambda = 510$ nm) [36]. As shown in Fig. 9, even after 4 cyclic runs, the optimized Fe-BDC/Fe-2MI exhibited high performance with a negligible loss in activity. Moreover, the leaching of Fe^{3+} from Fe-BDC/Fe-2MI during the photocatalytic process was also monitored. As shown in Fig. S7, after 90 min under visible light, the concentration of dissolved Fe^{3+} was ca. 0.28 mg/L. Imaging that the initial added Fe-BDC/Fe-2MI powder (10 mg) was totally dissolved in 100 mL reaction solution, the maximum concentration of dissolved Fe^{3+} was ca. 8.55 mg/L. Thus, the percentage of Fe^{3+} leaching was ca. 3.3%. Even after 10 h, the percentage was ca. 4.1%, indicating the high stability of Fe-BDC/Fe-2MI in aqueous media. Thus, the as-prepared Fe-BDC/Fe-2MI heterojunction with mixed organic ligands can be considered as a potential stable candidate for photocatalytic applications.

3.4. Proposed mechanism

In this study, the as-prepared Fe-BDC/Fe-2MI composite displayed an enhanced photocatalytic activity for Cr(VI) reduction. In order to clarify the intrinsic electronic properties, the Mott-Schottky curves of Fe-BDC and Fe-2MI were measured in a 0.5 M Na_2SO_4 solution. As shown in Fig. 10A-B, the estimated flat band potential was -0.3 V vs Ag/AgCl for Fe-BDC and -0.6 V vs Ag/AgCl for Fe-2MI, respectively. Whereas, the value for Fe-BDC/Fe-2MI composite was ca. -0.47 V vs Ag/AgCl (Fig. 10C). Further, the positive slop of Mott-Schottky curves indicated the n-type behavior of a semiconductor. Typically, for a n-type photocatalyst, the flat band potential was applied to indicate the CB (LUMO) position. Thus, the LUMO positions of Fe-BDC and Fe-2MI were estimated to be -0.1 V vs NHE and -0.4 V vs NHE, respectively. Considering the band gaps (E_g) of pure Fe-BDC (2.73 eV) and Fe-2MI (1.82 eV), the corresponding HOMO positions were estimated to be 2.63 eV and 1.42 eV, respectively. As shown in Fig. 10D, the HOMO-LUMO positions matched well with each other, and favored the formation of type II heterojunctions between Fe-BDC and Fe-2MI. In this way, the photo-generated e^-—h^+ pairs can be separated more efficiently.

4. Conclusions

In summary, novel Fe-BDC/Fe-2MI heterojunction was successfully fabricated via one-pot hydrothermal method using mixed ligands (H_2BDC and 2MI). Structural characterizations indicated that the presence of 2MI significantly affected the morphology and structure of Fe-BDC. Spindle-like MIL-88B(Fe) was obtained in the Fe-BDC/Fe-2MI composite; meanwhile, MIL-53(Fe) was identified in naked Fe-BDC without the presence of 2MI. As compared with single Fe-BDC and Fe-2MI, the optimized Fe-BDC/Fe-2MI composite exhibited the highest photocurrent response, lowest charge transfer resistance, and fastest surface reaction kinetics; this synergetic effect led to an boosted photocatalytic activity for Cr(VI) reduction. At a very low catalyst dosage (0.1 g/L) and approximately neutral pH (pH 4.5), it was observed that Cr (VI) can be completely reduced within 60 min. Moreover, the as-prepared Fe-BDC/Fe-2MI displayed high stability in cyclic runs. Thus, for the photocatalytic disposal of Cr(VI)-containing wastewater, this study provides a simple strategy for augmenting the performance via engineering the structure of Fe-MOFs with mixed ligands.

CRediT authorship contribution statement

Qin He: Data curation, Formal analysis, Writing - original draft.

Yangjie Fu: Data curation. **Xueying Ge:** Data curation. **Abdullah M. Al-Enizi:** Writing - review & editing. **Ayman Nafady:** Writing - review & editing. **Qi Wang:** Conceptualization, Methodology, Supervision, Writing - review & editing. **Shengqian Ma:** Conceptualization, Methodology, Supervision, Writing - review & editing.

Declaration of Competing Interest

The authors declare that they have no known competing financial interests or personal relationships that could have appeared to influence the work reported in this paper.

Appendix A. Supporting information

Supplementary data associated with this article can be found in the online version at doi:10.1016/j.jece.2021.105961.

References

[1] J. Schneider, M. Matsuoka, M. Takeuchi, J. Zhang, Y. Horiuchi, M. Anpo, D. W. Bahnemann, Understanding TiO2 photocatalysis: mechanisms and materials, Chem. Rev. 114 (2014) 9919–9986.

[2] M.N. Chong, B. Jin, C.W.K. Chow, C. Saint, Recent developments in photocatalytic water treatment technology: A review, Water Res. 44 (2010) 2997–3027.

[3] J.D. Xiao, H.L. Jiang, Metal–organic frameworks for photocatalysis and photothermal catalysis, Acc. Chem. Res 52 (2019) 356–366.

[4] X. Ma, L. Wang, Q. Zhang, H.L. Jiang, Switching on the photocatalysis of metal–organic frameworks by engineering structural defects, Angew. Chem. Int. Ed. 58 (2019) 12175–12179.

[5] C.C. Chen, W.H. Ma, J.C. Zhao, Semiconductor-mediated photodegradation of pollutants under visible-light irradiation, Chem. Soc. Rev. 39 (2010) 4206–4219.

[6] X.J. Lang, X.D. Chen, J.C. Zhao, Heterogeneous visible light photocatalysis for selective organic transformations, Chem. Soc. Rev. 43 (2014) 473–486.

[7] J. He, Y. Zhang, J. He, X. Zeng, X. Hou, Z. Long, Enhancement of photoredox catalytic properties of porphyrinic metal–organic frameworks based on titanium incorporation via post-synthetic modification, Chem. Commun. 54 (2018) 8610–8613.

[8] M.A. Nasalevich, D.V.M. Van, F. Kapteijn, Gascon, Metal–organic frameworks as heterogeneous photocatalysts: advantages and challenges, CrystEngComm 16 (2014) 4919–4926.

[9] D. Wang, M. Wang, Z. Li, Fe-based metal–organic frameworks for highly selective photocatalytic benzene hydroxylation to phenol, ACS Catal. 5 (2015) 6852–6857.

[10] E.M. Dias, C. Petit, Towards the use of metal–organic frameworks for water reuse: a review of the recent advances in the field of organic pollutants removal and degradation and the next steps in the field, J. Mater. Chem. A. 3 (2015) 22484–22506.

[11] J. Bedia, V. Muelas-Ramos, M. Peñas-Garzón, A. Gómez-Avilés, J.J. Rodríguez, C. Belver, A review on the synthesis and characterization of metal organic frameworks for photocatalytic water purification, Catalysts 9 (2019) 52.

[12] C.C. Wang, X.D. Du, J. Li, X.X. Guo, P. Wang, L. Zhang, Photocatalytic Cr(VI) reduction in metal-organic frameworks: A mini-review, Appl. Catal. B Environ. 193 (2016) 198–216.

[13] J.D. Xiao, D. Li, H.L. Jiang, Metal-organic frameworks for photocatalysis, Sci. Sin. Chim. 48 (2018) 1058–1075.

[14] J.L. Wang, C. Wang, W. Lin, Metal–organic frameworks for light harvesting and photocatalysis, ACS Catal. 2 (2012) 2630–2640.

[15] J.D. Xiao, L. Han, J. Luo, S.H. Yu, H.L. Jiang, Integration of plasmonic effects and schottky junctions into metal–organic framework composites: steering charge flow for enhanced visible-light photocatalysis, Angew. Chem. Int. Ed. 57 (2018) 1103–1107.

[16] H.C. Zhou, S. Kitagawa, S. Metal-organic frameworks (MOFs), Chem. Soc. Rev. 43 (2014) 5415–5418.

[17] L. Jiao, Y. Wang, H.L. Jiang, Q. Xu, Metal–organic frameworks as platforms for catalytic applications, Adv. Mater. 30 (2018), 1703663.

[18] M. Alvaro, E. Carbonell, B. Ferrer, F.X. Llabres, I. Xamena, H. Garcia, Semiconductor behavior of a metal-organic framework (MOF), Chem. Eur. J. 13 (2007) 5106–5112.

[19] L. Shen, R. Liang, M. Luo, F. Jing, L. Wu, Electronic effects of ligand substitution on metal–organic framework photocatalysts: the case study of UiO-66, Phys. Chem. Chem. Phys. 17 (2015) 117–121.

[20] J. Gascon, M.D. Hernández-Alonso, A.R. Almeida, G.P.M. Van-Klink, F. Kapteijn, G. Mul, Isoreticular MOFs as efficient photocatalysts with tunable band gap: an operando FTIR study of the photoinduced oxidation of propylene, ChemSusChem 1 (2008) 981–983.

[21] J.X. Liu, M.Y. Gao, W.H. Fang, L. Zhang, J. Zhang, Bandgap engineering of titanium–oxo clusters: labile surface sites used for ligand substitution and metal incorporation, Angew. Chem. Int. Ed. 55 (2016) 5160–5165.

[22] R. Liang, F. Jing, L. Shen, N. Qin, L. Wu, MIL-53(Fe) as a highly efficient bifunctional photocatalyst for the simultaneous reduction of Cr(VI) and oxidation of dyes, J. Hazard. Mater. 287 (2015) 364–372.

[23] F. Jing, R. Liang, J. Xiong, R. Chen, S. Zhang, Y. Li, L. Wu, MIL-68(Fe) as an efficient visible-light-driven photocatalyst for the treatment of a simulated waste-water contain Cr(VI) and Malachite Green, Appl. Catal. B: Environ. 206 (2017) 9–15.

[24] B. Xu, H. Yang, Y. Cai, H. Yang, C. Li, Preparation and photocatalytic property of spindle-like MIL-88B(Fe) nanoparticles, Inorg. Chem. Commun. 67 (2016) 29–31.

[25] H. Wang, L. Zhang, Z. Chen, J. Hu, S. Li, Z. Wang, J. Liu, X. Wang, Semiconductor heterojunction photocatalysts: design, construction, and photocatalytic performances, Chem. Soc. Rev. 43 (2014) 5234–5244.

[26] A.A. Oladipo, M.I.L.-53 (Fe)-based, photo-sensitive composite for degradation of organochlorinated herbicide and enhanced reduction of Cr(VI), Process. Saf. Environ. Prot. 116 (2018) 413–423.

[27] R. Panda, S. Rahut, J.K. Basu, Preparation of a Fe2O3/MIL-53(Fe) composite by partial thermal decomposition of MIL-53(Fe) nanorods and their photocatalytic activity, Rsc. Adv. 6 (2016) 80981–80985.

[28] Y. Han, C. Bai, L. Zhang, J. Wu, H. Meng, J. Xu, Y. Xu, Z. Liang, X. Zhang, A facile strategy for fabricating AgI–MIL-53(Fe) composites: superior interfacial contact and enhanced visible light photocatalytic performance, New. J. Chem. 42 (2018) 3799–3807.

[29] L. Xie, Z. Yang, W. Xiong, Y. Zhou, J. Cao, Y. Pen, X. Li, C. Zhou, R. Xu, Y. Zhang, Construction of MIL-53(Fe) metal-organic framework modified by silver phosphate nanoparticles as a novel Z-scheme photocatalyst: visible-light photocatalytic performance and mechanism investigation, Appl. Surf. Sci. 465 (2019) 103–115.

[30] S.G. Khasevani, M.R. Gholami, Novel MIL-88A/g-C3N4 nanocomposites: fabrication, characterization and application as a photocatalyst, Inorg. Chem. Commun. 102 (2019) 221–228.

[31] X. Du, X. Yi, P. Wang, J. Deng, C.C. Wang, Enhanced photocatalytic Cr(VI) reduction and diclofenac sodium degradation under simulated sunlight irradiation over MIL-100(Fe)/g-C3N4 heterojunctions, Chin. J. Catal. 40 (2019) 70–79.

[32] Q. Zha, F. Yuan, G. Qin, Y. Ni, Cobalt-based MOF-on-MOF two-dimensional heterojunction nanostructures for enhanced oxygen evolution reaction electrocatalytic activity, Inorg. Chem. 59 (2020) 1295–1305.

[33] L. Liu, L. Zhang, F. Wang, K. Qi, H. Zhang, X. Cui, W. Zheng, Bi-metal–organic frameworks type II heterostructures for enhanced photocatalytic styrene oxidation, Nanoscale 11 (2019) 7554–7559.

[34] Y. Gu, Y. Wu, L. Li, W. Chen, F. Li, S. Kitagawa, Controllable modular growth of hierarchical MOF-on-MOF architectures, Angew. Chem. Int. Ed. 56 (2017) 15658–15662.

[35] D.K. Panchariya, R.K. Rai, E. Anil Kumar, S.K. Singh, Core–shell zeolitic imidazolate frameworks for enhanced hydrogen storage, ACS Omega 3 (2018) 167–175.

[36] H.L. Tian, T. Araya, R.P. Li, Y.F. Fang, Y.P. Huang, Removal of MC-LR using the stable and efficient MIL-100/MIL-53 (Fe) photocatalyst: the effect of coordinate immobilized layers, Appl. Catal. B: Environ. 254 (2019) 371–379.

[37] J. Liu, F. Yang, Q. Zhang, W. Chen, Y. Gu, Q. Chen, Construction of hierarchical Fe3O4@HKUST-1/MIL-100(Fe) microparticles with large surface area through layer-by-layer deposition and epitaxial growth methods, Inorg. Chem. 58 (2019) 3564–3568.

[38] F. Nouar, T. Devic, H. Chevreau, N. Guillou, E. Gibson, G. Clet, M. Daturi, A. Vimont, J.M. Grenèche, M.I. Breeze, R.I. Walton, P.L. Llewellyn, C. Serre, Tuning the breathing behaviour of MIL-53 by cation mixing, Chem. Commun. 48 (2012) 10237–10239.

[39] P. Horcajada, T. Chalati, C. Serre, B. Gillet, C. Sebrie, T. Baati, J.F. Eubank, D. Heurtaux, P. Clayette, C. Kreuz, J.S. Chang, Y.K. Hwang, V. Marsaud, P. N. Bories, L. Cynober, S. Gil, G. Férey, P. Couvreur, R. Gref, Porous metal–organic-framework nanoscale carriers as a potential platform for drug delivery and imaging, Nat. Mater. 9 (2010) 172–178.

[40] Q. Wang, C. Zhang, H. Wu, Q. Gao, R. Duan, C. Chen, J, Fabrication of β-phase AgI and Bi2O3 co-decorated Bi2O2CO3 heterojunctions with enhanced photocatalytic performance, J. Colloid Inter. Sci. 547 (2019) 1–13.

[41] Q. Wang, X. Shi, J. Xu, J.C. Crittenden, E. Liu, Y. Zhang, Y. Cong, Highly enhanced photocatalytic reduction of Cr(VI) on AgI/TiO2 under visible light irradiation: influence of calcination temperature, J. Hazard. Mat. 307 (2016) 213–220.

[42] Y. Cong, Y. Ji, Y. Ge, H. Jin, Y. Zhang, Q. Wang, Fabrication of 3D Bi2O3-BiOI heterojunction by a simple dipping method: highly enhanced visible-light photoelectrocatalytic activity, Chem. Eng. J. 307 (2017) 572–582.

[43] Q. Wang, Q. Gao, H. Wu, Y. Fan, D. Lin, Q. He, Y. Zhang, Y. Cong, In situ construction of semimetal Bi modified BiOI-Bi2O3 film with highly enhanced photoelectrocatalytic performance, Sep. Purif. Technol. 226 (2019) 232–240.

[44] Q. Gao, D. Lin, Y. Fan, Q. He, Q. Wang, Visible light induced photocatalytic reduction of Cr(VI) by self-assembled and amorphous Fe-2MI, Chem. Eng. J. 374 (2019) 10–19.

[45] P.L. Llewellyn, G. Maurin, T. Devic, N. Rosenbach, S. Bourrelly, C. Serre, D. Vincent, S. Loera-Serna, Y. Filinchuk, G. Férey, Complex adsorption of short linear alkanes in the flexible metal-organic-framework MIL-53(Fe), J. Am. Chem. Soc. 131 (2009) 13002–13008.

[46] W. Huang, L. Ning, X. Zhang, M. Wu, L. Tang, Metal organic framework g-C3N4/MIL-53(Fe) heterojunctions with enhanced photocatalytic activity for Cr(VI) reduction under visible light, Appl. Surf. Sci. 425 (2017) 107–116.

[47] L. Shi, T. Wang, H. Zhang, K. Chang, X. Meng, H. Liu, J. Ye, An amine-functionalized iron(III) metal–organic framework as efficient visible-light photocatalyst for Cr(VI) reduction, Adv. Sci. (Weinh.) 2 (2015), 1500006.

[48] C. Wu, Q. Liu, R. Chen, J. Liu, H. Zhang, R. Li, K. Takahashi, P. Liu, J. Wang, Fabrication of ZIF-8@SiO2 micro/nano hierarchical superhydrophobic surface on AZ31 magnesium alloy with impressive corrosion resistance and abrasion resistance, ACS Appl. Mater. Interf. 9 (2017) 11106–11115.

[49] J.P. Vimlesh Chandra, Y. Chun, J.W. Lee, I.C. Hwang, K.S. Kim, Water-dispersible magnetite-reduced graphene oxide composites for arsenic removal, ACS Nano. 4 (2010) 3979–3986.

[50] Q. Wang, Q. Gao, A.M. Al-Enizi, A. Nafady, S. Ma, Recent advances in MOF-based photocatalysis: environmental remediation under visible light, Inorg. Chem. Front. 7 (2020) 300–339.